Corrosion Science 182 (2021) 109265

Contents lists available at ScienceDirect

Corrosion Science

journal homepage: www.elsevier.com/locate/corsci

Influence of H_2S on the pitting corrosion of 316L stainless steel in oilfield brine

J. Hesketh [a], E.J.F. Dickinson [a], M.L. Martin [b], G. Hinds [a], A. Turnbull [a,*]

[a] National Physical Laboratory, Hampton Road, Teddington, TW11 0LW, United Kingdom
[b] NIST, 325 Broadway, MS 647, Boulder, CO, 80305, United States

ARTICLE INFO

Keywords:
Stainless steel
SEM, TEM
Pitting corrosion

ABSTRACT

Coupon immersion tests were performed on 316L stainless steel in a simulated oilfield environment to evaluate the effect of H_2S partial pressure on pit depth and density. Pitting was most significant at intermediate partial pressures of H_2S, for which free H_2S in the pit solution is maximised. Inhibition of pitting at higher partial pressures is attributed to blocking of the pit surface by metal sulphide phases. The key role of pH in the pit solution is to determine the solubility of metal sulphides and the availability of free H_2S to adsorb on the reacting pit surface and sustain activity.

1. Introduction

In the oil and gas industry, corrosion resistant alloy (CRA) pipelines, linings, and fixtures are deployed for operating conditions considered too severe for application of carbon steel with chemical inhibition, or where the CRAs provide the most practical economic choice for system management. The environments tend to be mildly acidic, with a high concentration of chlorides, and may contain H_2S. In combination with an elevated temperature, these conditions are highly corrosive and capable of inducing stress corrosion cracking (SCC). As such, materials specified for service must be shown to be resistant to SCC through laboratory qualification testing according to standards such as NACE MR0175/ISO 15156 [1]. Tests for resistance to SCC typically involve exposing specimens of the stressed alloy to conditions broadly comparable to or more conservative than those encountered in service and performing post-test analysis to detect evidence of SCC.

The potential limitations of this approach are the relatively short timescale and small-scale nature of most testing, the idealised and variable surface preparation of test specimens in some cases, and uncertainty as to whether the laboratory environmental exposure conditions are sufficiently representative of service environments. While service experience of alloy performance can compensate to an extent, the complex interplay of variables, such as salt composition and concentration, gas pressure and composition, temperature, active electrochemical processes, and stress mode, can challenge confidence in applying laboratory test data to materials selection and design for new, often more aggressive, oilfields. Confidence is undermined by the lack of fundamental understanding of the cracking mechanism and of the relative significance of different variables in controlling the cracking process. The consequences can be over-conservatism and over-specification of material in design or, conversely, and more concerningly, under-specification, resulting in catastrophic failure of in-service components. Improved understanding of the underlying mechanisms would lead to more reliable interpretation and application of test results, leading to reduced costs and safer operation.

In chloride solution, stress corrosion cracking of austenitic stainless steels such as 316L stainless steel (SS) is usually preceded by pitting corrosion, both in aerated solution [2,3] and in sour (H_2S-containing) environments [4–7]. However, pits do not necessarily lead to the formation of cracks; whether they do so will depend on pit size, pit geometry and pit growth rate. The associated uncertainty has resulted in a lack of guidance on the interpretation of short-term tests for SCC of CRAs in sour environments in which the material exhibits corrosion pits but without cracks. At NACE International meetings on standardisation, this has led to discussion of a threshold pit size for acceptance or rejection of a material, but no consensus. In the absence of detailed insight, such a concept has been excluded from current standards and it is left to the end user to define their acceptance criteria.

To allow material selection decisions to be made on a more informed basis, better understanding of the pitting mechanism on 316L SS in sour conditions is required. Pits initiate at inhomogeneities such as inclusions and physical defects, with the latter becoming more significant for low

* Corresponding author.
E-mail address: alan.turnbull@npl.co.uk (A. Turnbull).

https://doi.org/10.1016/j.corsci.2021.109265
Received 27 October 2020; Received in revised form 12 January 2021; Accepted 14 January 2021
Available online 18 January 2021

sulphur containing steels with less refinement of the surface finish [7,8]. Ferrite stringers could also provide a site for localised attack. Sophisticated surface analytical techniques such as nanoSIMS and XPS have shown that exposure to H_2S-saturated brine leads to a high uptake of both sulphide and chloride into the oxide layer [9–14]. It has been proposed [12] that sulphide and chloride in the film may act synergistically, whereby the integration of sulphide into the passive film facilitates further infiltration by chloride and enhances initiation of pits at surface inhomogeneities. This would explain the more ready breakdown of the passive film in H_2S-containing solutions. However, the role of H_2S in sustaining propagation of pits in stainless steels has been less well characterised since the introduction of the concept proposed by Mat and Newman [15] and by Marcus [16] of sulphur species retarding repassivation and sustaining activity of the pit surface. Pit propagation in 316L SS has been studied in detail for many decades but the focus has been predominantly on aerated chloride environments. These conditions are very different to those encountered in sour oil and gas wells, which are essentially anoxic and contain hydrogen sulphide. As such, the well-developed, classical pitting models based on differential aeration and development of an acidic metal salt solution sustaining active corrosion in the pit [17] are not sufficient to predict the response of corrosion resistant alloys in these anoxic conditions.

To understand in greater detail the impact of H_2S on pit development in 316L SS, corrosion coupon exposure tests were conducted in simulated oilfield brines for several partial pressures of H_2S (balance CO_2) at two pH values. Supporting thermodynamic analysis was undertaken to rationalise the observations in the context of H_2S depletion in the pit, as proposed by Mat and Newman [15]. Test conditions were selected to be close to the pass/fail boundary with respect to resistance to SCC, guided by previous studies on SCC of 316L SS in H_2S environments [7].

2. Material characterisation

All testing was performed on coupons prepared from the mid-thickness of a 15 mm thick UNS S31603 (316L SS) plate, whose composition is shown in Table 1. The alloy has an equiaxed austenitic grain structure with delta ferrite bands. Identification of δ-ferrite was confirmed using scanning electron microscopy (SEM) and electron backscatter diffraction (EBSD), as shown in Fig. 1. In preparing the sample for EBSD imaging, the following procedure was used: specimens were cut to size using a precision saw; hot-mounted in phenolic resin; ground with SiC paper of decreasing coarseness (typically P400, P800, P1200 for ~2 min per stage); polished with diamond suspension (9 μm, 6 μm, 3 μm, 1 μm, 5–15 min per stage); finally polished with colloidal silica (2–15 min). The presence of scratches suggests polishing was not optimised but sufficient for purpose. The two grey regions in the SEM image are considered to be artefacts, possibly contamination in the SEM by carbon from a reduced raster while focusing. The small black dot could be an embedded particle or an inclusion. The sulphur content is very low (Table 1), so inclusion density would be low, but some MnS inclusions would be expected. The black dots in the ferrite phase in the EBSD images (Fig. 1d) could be other types of inclusion but were not investigated further. It should be noted that for these low sulphur stainless steels, physical defects from grinding can be the more common sites for pit initiation compared to MnS inclusions [7].

3. Experimental

3.1. Test coupons

The test coupon used had dimensions of 30 mm × 30 mm × 6 mm and contained a 6 mm diameter hole drilled into the face for ease of suspension from a polytetrafluoroethylene (PTFE) sample holder. The two large test surfaces of the coupon were prepared by first milling the surface of the supplied metal plate, then grinding a further 0.1 mm from each surface to achieve an average surface roughness Ra $\leq$ 0.2 μm, compatible with NACE standards such as TM0316 [18]. The deep surface grind was performed to remove the sub-surface material that had been deformed during the milling step. The sides of the coupon were ground to a similar nominal Ra value after cutting but without initial milling. Grinding of stainless steels to the required surface roughness has been shown to generate a surface nanocrystalline layer and subsurface plastic deformation with a depth dependent on the grinding procedure [7]. This is evidenced here also in Fig. 2, which shows that the near-surface microstructure still exhibited grain refinement (reflected in non-indexable grains, consistent with a nano-size grain structure), residual plastic deformation and a high-density of slip bands. Nano-sized grains are expected with grinding although the extent of sub-surface deformation and slip seems more representative of a machined surface.

3.2. Test solution

Test solution was prepared to represent produced water with a chloride concentration of 50,000 ppm, at a temperature of 110 °C. The solutions were buffered to a pH of either 4.0 or 4.5 under a standard set of conditions (1 bar CO_2, ambient temperature). The pH 4.0 solution was prepared by addition of 0.4 g/L CH_3COONa followed by HCl, and the pH 4.5 solution by addition of $NaHCO_3$, reflecting typical environments adopted in SCC testing according to TM0177 [19]. The in situ pH (value calculated at the test temperature) and buffering capacity, defined as $d[H^+]/d\text{pH}$, for each test are quoted in Table 2 as calculated using solubilities and acidity constants computed in the MTDATA thermodynamic and phase equilibria software [20]. The buffering capacity for an aqueous system is reported assuming that the concentrations of C atoms (from CO_2 dissolution, as CO_2, H_2CO_3, HCO_3^-, CO_3^{2-}) and S atoms (from H_2S dissolution, as H_2S, HS^-) are fixed at their pre-equilibrated value derived from the gas solubilities. A full derivation of the formulas used to predict in situ pH and the buffering capacity at the in situ pH is presented in Appendix A.

From the table, the CH_3COONa + HCl buffer system gives pH values close to the nominal value across the range of H_2S partial pressures. In contrast, the $NaHCO_3$ containing solution has an in situ pH about 0.5 units greater than the nominal value. Furthermore, the calculated buffering capacity of the CH_3COONa + HCl buffer is very consistent over the range of conditions and is substantially greater than that of the $NaHCO_3$ containing solution, whose buffering capacity is mostly derived from the dissolved gases and hence varies depending on the partial pressures of H_2S and CO_2.

3.3. Test procedure

The autoclaves used in the pitting corrosion tests were configured as shown in Fig. 3 and testing was conducted according to the following procedure:

Table 1
Composition of the 316L SS tested in this work (mass %).

C	Si	Mn	P	S	Cr	Ni	Mo	N	Fe
0.021	0.34	1.38	0.031	0.001	16.59	10.02	2.02	0.044	Bal.

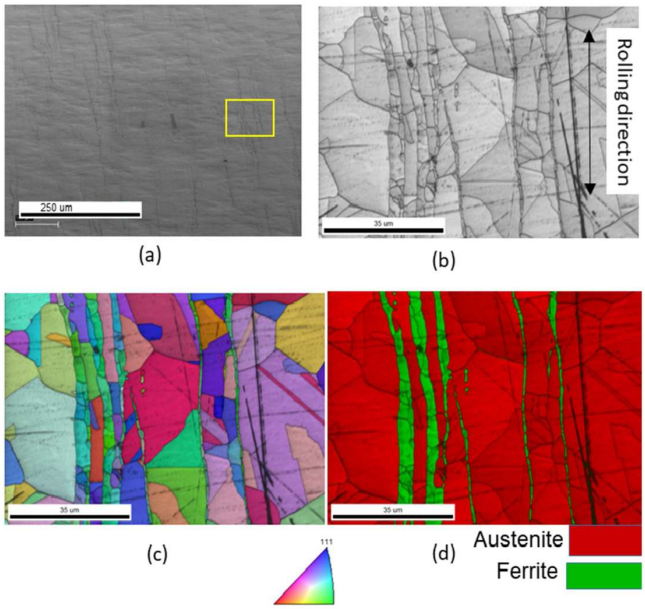

Fig. 1. Electron micrographs showing microstructure of 316L SS used in this work; (a) SEM image with boxed magnified image examined by EBSD: (b) image quality map (c) grain orientation map with cubic inverse pole figure colour scale superimposed on the image quality map and (d) phase map superimposed on the image quality map.

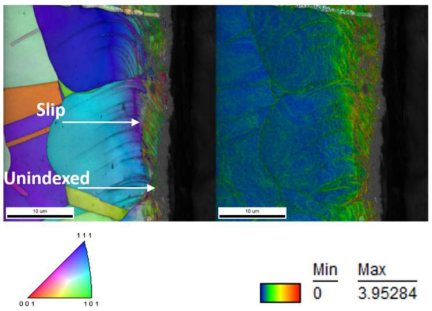

Fig. 2. Transverse cross-section of untested coupon specimen shown by EBSD orientation map (left) and EBSD grain reference orientation colour and map (right) superimposed on greyscale image quality maps.

1 Test coupons were degreased in acetone, rinsed in isopropanol and dried in air.
2 The coupons were suspended from a PTFE stand and were placed into the autoclave.
3 Test solution, in a separate vessel, was deaerated using high-purity nitrogen (>99.998 %) to reduce the dissolved oxygen concentration to less than 10 ppb according to a previously validated procedure [21]. The flow of nitrogen was used to simultaneously deaerate the autoclave containing the test coupons.
4 The deaerated solution was introduced to the deaerated autoclave using nitrogen pressure, following which the solution was sparged with nitrogen for a further hour to mitigate against oxygen ingress that may have occurred during transfer of the solution between vessels.
5 The solution was then sparged with a certified mixture of CO_2 and H_2S at the desired H_2S/CO_2 partial pressures at a rate of 100 mL/min for a minimum of 1 h per litre of test solution.
6 Autoclaves were heated, with the gas mixture still flowing, to a temperature of 57 °C, at which stage the gas flow through the submerged inlet was stopped to avoid blockage of the tube by sodium chloride deposits that often precipitate during gas flow through concentrated salt solution at elevated temperatures.
7 The autoclave was then heated to 110 °C and the H_2S/CO_2 gas mixture introduced to the head space of the autoclave using an inlet tube not submerged in the solution, at 100 mL/min for 1 h.
8 The inlet and outlet of the autoclave were sealed, and the test temperature was maintained to within ±0.5 °C for 30 days, with the exception of Test 2.7.
9 Upon completion of the test, the autoclave was vented and cooled back to ambient temperature then purged with high-purity nitrogen for 24 h before it was opened to remove the test coupons.
10 Test coupons were chemically cleaned using an aqueous solution of 50 % HCl +10 g/L of dibutylthiourea and rinsed in deionised water to remove the pit corrosion products. For coupons

Table 2
Test conditions for the pitting corrosion tests.

Test Number	pH_2S (bar)	pCO_2 (bar)	pH_{nom}	Time (days)	$[Cl^-]$ (ppm)	T (°C)	In situ pH*	$[H_2S_{(aq)}]$ (mM)*	Buffering capacity at in situ pH (mM)*
1.1	0.0	1.000					4.95	0	0.0212
1.2	0.010	0.990					4.94	0.334	0.0495
1.3	0.050	0.950	4.5	30	50,000	110	4.90	1.67	0.150
1.4	0.100	0.900					4.85	3.34	0.254
1.5	0.250	0.750					4.73	8.35	0.473
2.1	0.0	1.000					3.93	0	1.15
2.2	0.001	0.999					3.93	0.0334	1.15
2.3	0.010	0.990		30			3.93	0.334	1.15
2.4	0.050	0.950	4.0		50,000	110	3.92	1.67	1.16
2.5	0.100	0.900					3.92	3.34	1.17
2.6	0.250	0.750					3.91	8.35	1.21
2.7	0.010	0.990		1			3.93	0.334	1.13

* calculated as described in Appendix A, parameterised from MTDATA [20].

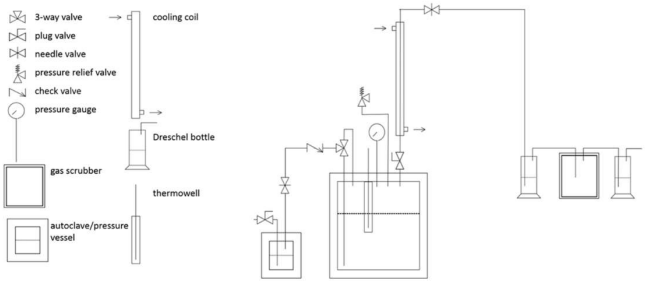

Fig. 3. Autoclave configuration used for all tests.

examined by SEM, the chemical cleaning step was not performed, and pits were rinsed with deionised water only.

11 Test coupons were examined for evidence of pitting corrosion using an Alicona Infinite Focus confocal microscope. The maximum observable depth and diameter of the major and minor axis of the opening of each pit was measured and recorded.

All corrosion coupons were tested in duplicate.

It was decided to fill and seal the autoclaves as opposed to charging them with gas continuously. This method is suitable when testing CRAs in the passive state as the rate of consumption of H_2S, through sulphide formation, is low and not anticipated to cause a significant depletion over the normal test duration of 30 days. Sparging the solution with the H_2S/CO_2 gas mixture prior to heating can introduce undesirable SCC in alloys that are sensitive to SCC at temperatures below the test temperature, and is advised against. In this work, where only pitting was investigated, it was adopted in order to avoid blockage of the gas inlet tube with salt, which occurs at higher temperatures even with humidified gas. However, when this is done with a mixture of two or more gases, the differential change in solubility of the gases can cause their relative partial pressures to change from that desired for the test. Step 7 above is designed to prevent this by replenishing the headspace of the autoclave with the gas mixture in the correct stoichiometric ratio. If this is not done, thermodynamic software [20] predicts that the H_2S partial pressure could be up to 20 % (calculated for a 50 % full autoclave) greater than expected from its stoichiometric ratio in the gas mixture.

4. Results

The results of the pitting corrosion tests performed at different

Table 3
Density and depth of pits formed during pitting corrosion coupon tests. The total area of the two faces is 18.00 cm^2 and that of the four sides is 7.20 cm^2.

Test	pH_2S (bar)	pH_{nom}	Test duration (days)	Density of pits (pits/cm^2)			Mean pit depth (μm)		Pit depth standard deviation (μm)	
				Total	Faces	Sides	Faces	Sides	Faces	Sides
1.1	0.0			0.12	0.17	0	13.7	n/a	1.70	n/a
1.2	0.010			2.02	2.39	1.11	13.8	15.1	3.65	7.59
1.3	0.050	4.5	30	0.79	0.39	1.81	17.6	31.6	3.58	27.7
1.4	0.100			1.23	1.22	1.25	22.9	23.6	12.2	14.7
1.5	0.250			1.27	0.83	2.36	16.8	24.6	8.03	16.7
2.1	0.0			0.63	0.94	0	21.6	n/a	8.50	n/a
2.2	0.001			0.63	0.89	0	14.1	n/a	2.20	n/a
2.3	0.010		30	1.90	0.33	5.83	23.0	84.1	7.19	102
2.4	0.050	4.0		3.02	0.11	10.28	32.0	39.3	3.00	19.9
2.5	0.100			0.40	0.22	0.83	31.5	21.0	22.8	8.98
2.6	0.250			0.63	0	2.22	n/a	18.6	n/a	2.87
2.7	0.010		1	0.24	0	0.83	n/a	78.8	n/a	13.8

concentrations of H_2S are given in Table 3. Features less than 10 μm in depth were ignored since untested coupons exhibited many pit-like physical defects of this scale. No evidence of crevice attack at the PTFE support was apparent. Since the surface preparation and microstructural orientation are different for the sides and faces of the coupon, pit distributions have been analysed separately for each.

Figs. 4 and 5 show the measured distribution of pit depths for the 30-day tests buffered to a pH_{nom} of 4.5 and 4.0 respectively. Pitting was observed on all surfaces but with the sides of the corrosion coupons tending to be a little more susceptible than the faces, albeit with significant variability in that respect. Pits that formed on the edges of coupons were clustered to an extent, but on the face they appeared randomly distributed. From the table and figures, it is evident that there is not a simple relationship between the severity of pitting and the bulk concentration of H_2S. At each pH value the greatest number of pits and the deepest pits formed at intermediate H_2S concentrations. Furthermore, the test performed for just 1 day in pH_{nom} 4.0 brine with 0.01 bar H_2S exhibited maximum pit depths comparable to the test performed in the same environment for 30 days, albeit the pits were fewer in number. This suggests that the pit growth rate was rapid initially, but the growth rate then declined significantly, or the pit growth arrested prior to test termination.

Visual inspection of the pits following testing revealed that they contained large amounts of black corrosion deposit. The nature of this deposit was investigated using SEM and energy dispersive X-ray (EDX) spectroscopy to map the cross-section of selected corrosion pits. Fig. 6 shows an SEM image of the cross-section of a corrosion pit, formed on the side of a coupon tested in 0.01 bar H_2S at pH 4.0. The pit is quite open compared to the transport-constraining bulbous shape typical of pitting of stainless steel in aerated chloride environments. There is irregularity in the pit surface, most notably associated with the location of stringers.

More detailed EDX point scans were taken at several locations, as shown in Fig. 7, and used for elemental quantification, the results of which are given in Table 4. The presence of the stringers in the bulk matrix can clearly be observed from the EDX maps, which show an abundance of Cr and a depletion of Ni. The precipitate within the pit was predominately a mixture of chromium, oxygen, nickel and sulphur, with a strong overlap between the nickel and sulphur signal and a strong overlap between the chromium and oxygen signal, suggesting the presence of nickel sulphide and chromium oxide. Iron was detected suggesting the presence of iron oxide/sulphide also. In principle, the species solubility and precipitate composition could be affected by the

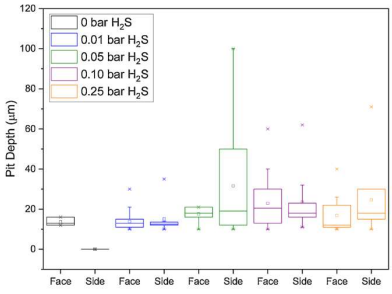

Fig. 4. Distribution of pit depths across face and side of corrosion coupons tested for 30 days at pH 4.5_{nom}, 50,000 ppm Cl^-, 110 °C under different H_2S partial pressures at a total pressure of 1 bar (balance CO_2). Range is indicated by the stars, square symbol indicates the mean, rectangular box indicates the median and quartiles whist the vertical lines indicate the 10th to 90th percentiles.

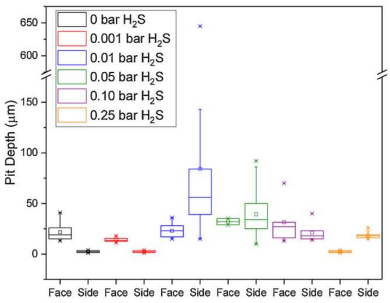

Fig. 5. Distribution of pit depths across face and side of corrosion coupons tested for 30 days at pH 4.0_{nom}, 50,000 ppm Cl^-, 110 °C under different H_2S partial pressures at a total pressure of 1 bar (balance CO_2). Range is indicated by the stars, square symbol indicates the mean, rectangular box indicates the median and quartiles whist the vertical lines indicate the 10th to 90th percentiles. Note the break in ordinate.

cooling to ambient temperature after the test. However, the observed dependence of pit size on H_2S partial pressure makes it far more likely that all of the precipitation occurred at the test temperature. A surprising observation from the EDX measurements was the absence of chloride, which could not be discerned above the noise level. Soluble chloride species are likely to have been washed out during treatment of the specimen post-test. The SEM image shows the presence of un-corroded stringers running top to bottom throughout the pit. Selective area electron diffraction (SAED) was performed on a TEM slide fabricated from one of the stringers, which confirmed that it had a BCC structure, consistent with it being δ-ferrite (Fig. 8).

SEM imaging on the face of a coupon showed no evidence of delta ferrite due to the orientation of the pit relative to the rolling direction. However, the pattern of corrosion at the base of the pit, with relatively sharp features evident, suggests possible preferential attack.

5. Discussion

5.1. Pit development in anoxic solution containing H_2S

Several questions arise from this study. Why is pit propagation enhanced by the presence of H_2S? Why are the deepest and most plentiful pits observed at intermediate partial pressures of H_2S? Why is pitting more severe at the higher partial pressures of H_2S for pH_{nom} 4.5, compared to the more acidic pH_{nom} 4.0?

Electrochemical measurements by Kahyarian and Nesic [22] do not tend to support the role of H_2S as a significant cathodic reactant in acidic environments of relevance to this study, except by acting as a source of hydrogen ions through its action as a buffer (see further discussion below). The analysis in this recent work has also cast doubt on prior work identifying a significant role for H_2S as a cathodic reactant on 316L SS [23]. Although our more recent cathodic polarisation measurements [24] suggest that at 0.01 bar H_2S (but not 0.1 bar) there is an additional cathodic reaction close to the open circuit potential, the positive shift in the potential relative to the H_2S-free solution was small, supporting the perspective that H_2S does not act as a major oxidant in driving the pitting process. Therefore, in the de-aerated sour environment, we consider the principal cathodic reaction to be hydrogen ion reduction:

$$H^+ + e^- \rightleftharpoons \frac{1}{2}H_2 \quad (1)$$

Correspondingly, the free corrosion potential in mildly acidic

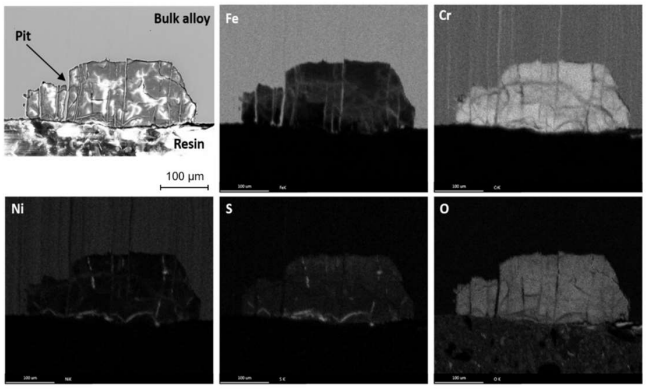

Fig. 6. SEM image of corrosion pit cross-section (top left), and corresponding EDX elemental maps. The pit was formed in 0.01 bar H_2S, pH 4.0, 50,000 ppm Cl^-, 110 °C and formed on the side of the test coupon.

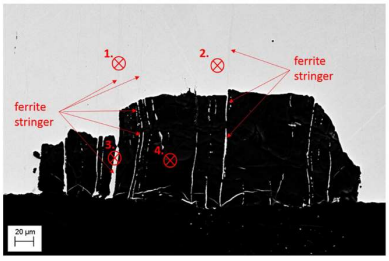

Fig. 7. Backscattered electron image of a pit cross-section highlighting locations where quantitative EDX point scans were made. The pit was formed in 0.01 bar H_2S, pH 4.0_{nom}, 50,000 ppm Cl^-, 110 °C and formed on the side of the test coupon.

Table 4
SEM-EDX quantification from point scans taken as shown in Fig. 7.

Area	Description	Cr	Fe	O	S	Mn	Mo	Ni
material spec.	bulk	16.8	69			1.3	2.0	10.0
1	ferrite in bulk	25.5	67.5			1.9	1.4	3.6
2	bulk	17.8	72.9				0.4	9.0
3	ferrite in pit	26.3	67.9			1.1	1.0	3.8
4	deposit in pit	49.5	29.9	13.6	3.0	0.8		3.2

environments of pH 4 or above can be up to several hundred mV more negative (typically about −0.4 V SCE [24]) than that for aerated solution. By implication, there is a decreased electrochemical driving force for metal dissolution and an increased driving force for cathodic reduction compared to aerated solution. The consumption of protons in the cathodic process would not be conducive to achieving very acidic concentrated metal chloride solutions in pits, as would be the case in aerated solution. Despite the lower corrosion potential of 316L SS in these oxygen-free mildly acidic solutions, substantial pitting does occur in the presence of H_2S, suggesting that the role of H_2S is primarily that of a chemical agent rather than an electrochemical agent.

In oilfield brines, the depassivation pH of duplex stainless steel was observed to increase from 1.2 in sweet conditions (no H_2S) to 2.2 and 3.2 at H_2S partial pressures of 0.01 bar and 1 bar, respectively [25,26]. This suggests that pit growth in the presence of H_2S can be sustained in a pit chemistry significantly less acidic than in aerated solution. It raises the question of the extent of the acidity in the pit solution and the process by which H_2S undermines repassivation.

H_2S is a weak buffer (pK_a 7) that through dissociation restrains an increase in pH:

$$H_2S \rightleftharpoons HS^- + H^+ \quad (2)$$

However, in the experimental testing on industrially relevant brines reported herein, and in contrast to some prior studies [10], buffering is also provided by acetate ions (pH 4 tests) and bicarbonate ions. Acetate ions will tend to resist a decrease in pH. Both ions will also preferentially migrate into the pit (compared to the neutral H_2S molecule) to balance the charge associated with the dissolving metal ions. In concentrated chloride solution, however, the potential gradient in the pit is likely to be small, and the effect of ion migration of second order with respect to diffusion of these ions. The key point is that the role of H_2S as a buffer in the pit will not be significant.

There has to be a specific role for H_2S in the pit propagation process that is not reliant on very acidic pit chemistry. The most likely mechanism for stainless steel, as proposed by Mat and Newman [15], is that sulphur species adsorbed on the pit surface sustain activity and retard repassivation, although at the low potential of about −0.4 V SCE associated with these test conditions it is unlikely that elemental sulphur plays a role. What is less clear is the specific pit chemistry required to maintain the steel in the active state as a function of pit size, corrosion potential and dissolved H_2S concentration. Based on the Mat and Newman concept, there has to be a sustained supply of H_2S to the evolving pit surface to maintain active behaviour. If the H_2S is consumed by reaction in the pit, this supply will be constrained and the pit may repassivate or its growth rate reduced. While H_2S can dissociate in the buffering process in response to hydrogen ion reduction, this dissociation does not correspond to a net consumption of S-containing species, and only to an alteration in the ratio of H_2S to HS^- as a function of local pH at different pit depths. Accordingly, the only process that irreversibly consumes H_2S after its transport into the pit will be reaction with metal ions, or direct reaction with the metal itself, to form the sulphide. For

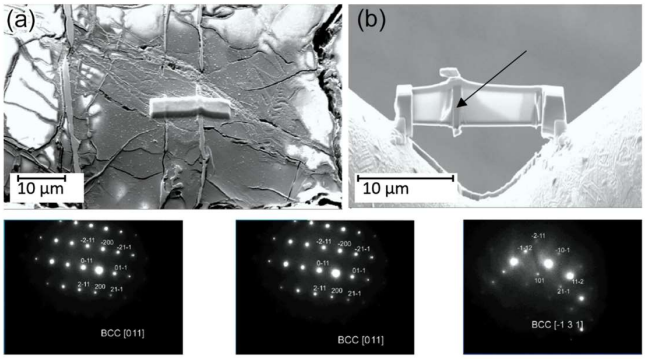

Fig. 8. TEM slide preparation by focused ion beam SEM (a), TEM slide containing stringer (b), and SAED patterns taken from stringer.

carbon steel, there is debate as to whether the metal sulphide is formed by dissolution of metal ions followed by precipitation from the (supersaturated) solution at nucleation sites, or by direct reaction of H_2S with the metal surface as proposed by Smith [27]. For stainless steel, little detailed insight is available in the reported experiments in the literature, but as the growing pit is in the active state, both processes may be feasible concurrently. Irrespective of the mechanism, formation of the sulphide at the base of a pit will lower the quantity of freely available H_2S for adsorption and reaction, the amount of freely available H_2S being then a balance of diffusion and reaction rates. With increasing pit depth, this balance can change, and retardation of growth rate could follow. This may explain the observations from the 1-day exposure experiments with maximum values similar to those after 30 days, suggesting repassivation or a sharply reduced pit growth rate. Increasing the concentration of H_2S might be expected to increase the availability of H_2S, and, in simple terms, lead to an increased pit growth rate. However, this ignores the more extensive formation of sulphides at higher H_2S concentration, and the consequent constraint to H_2S transport and reaction kinetics on the pit surface.

To illustrate the balance of effects for varying pH and H_2S concentration, we consider the solubility product for FeS, supposing the formation of metal sulphide within a pit to be governed thermodynamically by the local metal ion concentration, the pH and the concentration of H_2S. This is shown in Eq. 3, which describes the critical concentration of Fe^{2+} for precipitation of FeS. The same rationale would apply to the case of FeS formed by direct reaction between H_2S and the metal surface, as this process is thermodynamically indistinguishable from precipitation. Likewise, we do not suggest here that FeS is identically the phase of sulphide precipitate formed. Pyrite (FeS_2) and mixed phases such as mackinawite (FeS_{1-x}) may also form in sour aqueous environments [28, 29]. In the absence of freely available data for the precipitation mechanism and to avoid over-complication of the illustrative example, we adopt FeS as a representative example. Our discussion here is not intended to assert a specified chemistry for the inorganic sulphide deposits encountered in practice.

$$c_{Fe,crit,FeS} = \frac{K_{sp,FeS}}{c_{H_2S}} c_{H^+}^2 \quad (3)$$

where:

$c_{Fe,crit,FeS}$ is the critical concentration of Fe^{2+} for the onset of precipitation of H_2S as FeS

$K_{sp,FeS}$ is the solubility constant for FeS vs H_2S concentration, which for the test temperature is taken to be 471.7 [30]

c_{H+} is the concentration of H^+

c_{H2S} is the concentration of H_2S

The concentration of Fe^{2+}, $c_{Fe,crit,FeS}$, required to precipitate FeS for a given pH, defined in Eq. 3, is plotted for the concentrations of H_2S associated with the partial pressures used in the pitting tests at pH_{nom} 4.0 (Fig. 9). In this figure, Fe^{2+} concentrations, c_{Fe2+}, lying on or above the indicated line would be predicted to precipitate FeS at the corresponding partial pressure of H_2S. The solubility of FeS increases markedly with decreasing pH. It should be noted here that Fig. 9 plots the concentration of the aqueous species Fe^{2+} directly and is not a plot of the concentration of any particular Fe^{2+} salt (such as $FeCl_2$); therefore, common-ion effects are completely accounted for within Fig. 9. The 'salting-in' effect, whereby solubility product is a function of ionic strength, is not considered in this simple illustration.

High concentrations of dissolved metal ions and freely available H_2S for adsorption are attainable at low H_2S partial pressures but the amount of H_2S is small and the impact on pitting will be modest, especially when account is taken of the possible effect of Mo in desorbing sulphur species [15]. At the higher H_2S partial pressures (0.10 bar and 0.25 bar), precipitation is expected at Fe^{2+} concentrations well below 1 M. For a given concentration of metal ions, the precipitation of metal sulphide within a pit imposes a maximum limit on the concentration of dissolved H_2S.

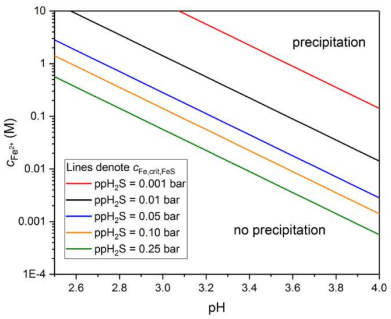

Fig. 9. Calculated conditions for precipitation of FeS as a function of Fe^{2+} concentration and pH, with precipitation onset for c_{Fe2+} above the corresponding line for each bulk H_2S concentration.

Hence, at higher bulk H_2S concentrations, the amount of precipitation that will occur within a given pit volume is greater, increasing the density of the precipitate. The corresponding limitation in mass transport of free H_2S caused by the high-density blocking precipitate may explain the inhibition of pitting observed. The blocking nature of high-density sulphide precipitates has been identified in previous work on hydrogen absorption [31]. Lower-density precipitates that form less rapidly at intermediate concentrations are expected to be inherently more porous and less able to block mass transport [32].

In a corrosion-resistant alloy, formation of less soluble sulphides, such as those of Mo and Ni, would exhibit comparable behaviour [26]. These sulphides are generally less soluble than FeS, but the metal ions are also present at lower concentration for a common corrosion rate, due to their lower stoichiometry in the steel compared to Fe. The significance of the FeS solubility for pit growth highlights the distinctive role of the solution pH in the pit in a way that is quite different from its role in aerated systems. There is also a coherent rationale for the pit growth and related pit dependence on the H_2S concentration, with an optimum H_2S concentration for pit growth just below or about the onset of precipitation. Also, too constrained a pit geometry would lead to a greater likelihood of precipitation so the pits that survive would tend to be more open than pits in stainless steel in aerated solution.

The results of the pitting tests indicated that for a pH_{nom} of 4.5, the most severe pitting was observed at H_2S partial pressures of 0.05 bar and 0.10 bar. At a pH_{nom} of 4.0, the most severe pitting was observed at H_2S partial pressures of 0.01 bar and 0.05 bar. The trend to more pitting with lower H_2S partial pressures was more pronounced for the tests performed at the lower pH, which exhibited very few and small pits at the highest partial pressure of H_2S (0.25 bar). The tests in the lower pH solution also indicated larger pits for the low to intermediate H_2S concentrations, suggesting that the expected more noble potential for the lower bulk solution pH was determining the dissolution kinetics, despite the greater buffering from the acetate ion. However, at higher concentrations of H_2S, pitting was more severe at pH_{nom} 4.5 compared to pH_{nom} 4.0. In this case it would appear that a lower pH was attainable in the pit with the less well buffered solution, which would then increase the solubility of the metal sulphides and allow more H_2S adsorption.

5.2. *Role of microstructure*

Pitting in 316L SS is strongly dependent on both microstructure and the extent of plastic deformation introduced by the manufacturing process used to produce the coupons [7,33,34]. The density of pits on the side faces of the coupons was greater and the pits larger than on the faces of the coupons (Figs. 4 and 5) despite the expectation of a less deformed surface.

The rapid growth of pits on the sides of the coupons may be explained with the aid of SEM cross-sections of the largest pits, which showed that pit growth was influenced by the steel microstructure. Transverse δ-ferrite stringers were visible in pits that initiated on the sides of coupons. When analysed by SEM-EDX, they were found to have chromium levels of ~26 %, which is greater than the ~17 % within the bulk and suggests that there would be associated chromium depletion in the austenite at the ferrite-austenite phase boundary. This is supported by the work of Sui et al. [35] who demonstrated that δ-ferrite present in 316L SS can sequester both Cr and Mo from the matrix to form a depleted zone, which under active corrosion leads to the formation of a micro-galvanic cell between the adjacent phases. Pits that initiated on the face of coupons might not be expected to propagate along the phase boundaries to any significant depth due to the longitudinal orientation of the δ-ferrite. However, previous work on the same batch of material, in a high H_2S simulated condensing environment in this case, showed that deep pits that initiated at the surface can propagate subsurface laterally by many millimetres [36], which presumably occurred when a pit intersected a δ-ferrite phase and propagated along the phase boundary between it and the matrix. The extent of this attack may have been specific to those environmental conditions, and perhaps would have been limited for the current high chloride test solutions, but the possibility that different sampling of material for the test coupons could induce such localised attack cannot be completely eliminated.

6. Conclusions

- The influence of dissolved H_2S concentration on the pit propagation of 316L SS is non-monotonic, with aggressivity being most significant at an intermediate concentration.
  - o At low concentration of H_2S, some pitting is observed, consistent with the proposition that adsorbed H_2S on the pit surface maintains an active surface, constraining the repassivation that might otherwise ensue in anoxic solution.
  - o At intermediate concentrations, pitting is more severe, reflecting the higher concentration of free H_2S. Formation of metal sulphides may occur to some extent, but the sulphide is considered to be porous and not sufficiently restrictive to active corrosion.
  - o At high concentration of H_2S, which might have been presumed to be most aggressive, pit development is significantly constrained; this is attributed to formation of protective dense sulphides, limiting metal dissolution and transport of H_2S for adsorption on the fresh surface. The growth of the pit is then stifled.
- The key role of pH in the pit solution in this anoxic system is in determining the solubility of metal sulphides and the availability of free H_2S to adsorb on the reacting pit surface and sustain activity; the more acidic the pit solution, the more soluble the iron sulphide, and the greater the impact of H_2S on pit propagation.

Data availability statement

The raw/processed data required to reproduce these findings cannot be shared at this time as the data also form part of an ongoing study.

CRediT authorship contribution statement

J. Hesketh: Conceptualization, Methodology, Formal analysis, Investigation, Data curation, Writing - original draft. **E.J.F. Dickinson:** Software, Writing - review & editing. **M.L. Martin:** Investigation. **G. Hinds:** Project administration, Funding acquisition, Supervision, Writing - review & editing. **A. Turnbull:** Conceptualization, Supervision, Writing - review & editing.

Declaration of Competing Interest

The authors declare no conflict of interest.

Acknowledgements

This work was supported by the National Measurement System of the United Kingdom Department for Business, Energy, and Industrial Strategy.

Appendix A

This appendix summarises the mathematical computation of in situ pH and buffering capacity for the brines studied in this work. In all stated equations, all the equilibrium constants are functions of ionic strength and temperature and are evaluated as such from MTDATA thermodynamic

software [20].

The brine is considered to contain the following dissolved ions:

- Inert electrolyte: Na^+, Cl^-
- Water ions: H^+, OH^-
- Carbon-containing species: CO_2, H_2CO_3, HCO_3^-, CO_3^{2-}
- Sulphur-containing species: H_2S, HS^- (S^{2-} is ignored for the pH range < 7)
- Organic acid species: AcOH, AcO^-

The NaCl solution equilibrated with the acid gases CO_2 and H_2S may have its pH modified by introducing strong acid/base (HCl / NaOH) and/or weak base (NaOAc, $NaHCO_3$).

Under any condition, a global electroneutrality constraint applies:

$$c_{Na} + c_H = c_{Cl} + c_{OH} + c_{HCO_3} + 2c_{CO_3} + c_{HS} + c_{AcO} \tag{A.1}$$

The constant contribution from dissolved NaCl is equal for both c_{Na} and c_{Cl} and can be removed, giving only contributions from added acids or bases:

$$c_{addn,wb} + c_H = c_{addn,sa} + c_{OH} + c_{HCO_3} + 2c_{CO_3} + c_{HS} + c_{AcO} \tag{A.2}$$

The hydroxide concentration is constrained by the self-ionisation equilibrium of water:

$$c_{OH} = \frac{K_w}{c_H} \tag{A.3}$$

The CO_2 and H_2S concentrations are constrained by the gas dissolution equilibria:

$$c_{CO_2} = c_{sat,CO_2} = K_{H,CO_2} p_{CO_2} \tag{A.4}$$

$$c_{H_2S} = c_{sat,H_2S} = K_{H,H_2S} p_{H_2S} \tag{A.5}$$

The carbonic acid concentration relates to the CO_2 concentration according to a hydration equilibrium:

$$c_{H_2CO_3} = \frac{c_{CO_2}}{K_{hyd,CO_2}} \tag{A.6}$$

The other carbon- and sulfur-containing species obey acid-base equilibria:

$$c_{HCO_3} = \frac{K_{a,H_2CO_3} c_{H_2CO_3}}{c_H} \tag{A.7}$$

$$c_{CO_3} = \frac{K_{a,HCO_3} c_{HCO_3}}{c_H} \tag{A.8}$$

$$c_{HS} = \frac{K_{a,H_2S} c_{H_2S}}{c_H} \tag{A.9}$$

The concentrations of acetic acid and acetate can be written in terms of the total added acetic acid/acetate buffer concentration, as follows:

$$c_{AcOH} = c_{AcOH,tot} \frac{c_H}{c_H + K_{a,AcOH}} \tag{A.10}$$

$$\begin{aligned} c_{AcO} &= c_{AcOH,tot} \frac{K_{a,AcOH}}{c_H + K_{a,AcOH}} \\ &= \frac{c_{AcOH,tot}}{c_H} \frac{K_{a,AcOH}}{1 + \frac{K_{a,AcOH}}{c_H}} \end{aligned} \tag{A.11}$$

Introducing these expressions into the electroneutrality balance gives:

$$\begin{aligned} &c_H - \left(c_{addn,sa} - c_{addn,wb}\right) = \\ &\frac{1}{c_H}\left(K_w + \frac{K_{a,H_2CO_3} K_{H,CO_2} p_{CO_2}}{K_{hyd,CO_2}}\left(1 + 2\frac{K_{a,HCO_3}}{c_H}\right) + K_{a,H_2S} K_{H,H_2S} p_{H_2S} + \frac{c_{AcOH,tot} K_{a,AcOH}}{1 + \frac{K_{a,AcOH}}{c_H}}\right) \end{aligned} \tag{A.12}$$

which is a nonlinear equation for c_H (and hence pH) that can be solved under known conditions.

For $pH_{nom} = 4.0$, a nominal temperature $T_{nom} = 23$ °C, and the resulting nominal strong acid addition to achieve pH = 4 is solved for this temperature with $p_{CO2,nom} = 1$ bar, $p_{H2S,nom} = 0$, $c_{addn,NaOAc,nom} = 5$ mM:

$$c_{\mathrm{addn,sa,nom}} = c_{\mathrm{H,appl}} + c_{\mathrm{addn,NaOAc,nom}}$$

$$-\frac{1}{c_{\mathrm{H,appl}}}\left(K_{\mathrm{w}} + \frac{K_{\mathrm{a,H_2CO_3}} K_{\mathrm{H,CO_2}} p_{\mathrm{CO_2,nom}}}{K_{\mathrm{hyd,CO_2}}}\left(1 + 2\frac{K_{\mathrm{a,HCO_3^-}}}{c_{\mathrm{H,appl}}}\right) + \frac{c_{\mathrm{addn,NaOAc,nom}} K_{\mathrm{a,AcOH}}}{1 + \frac{K_{\mathrm{a,AcOH}}}{c_{\mathrm{H,appl}}}}\right) \tag{A.13}$$

Then the solution is re-equilibrated with its new conditions ($T = 110$ °C, p_{CO2} and p_{H2S} from experimental conditions). The mineral content molalities (Na^+, Cl^-, AcO^-) are assumed to remain constant during re-equilibration. Hence:

$$c_{\mathrm{addn,sa}} = c_{\mathrm{addn,sa,nom}} \frac{\rho}{\rho_{\mathrm{nom}}} \tag{A.14}$$

$$c_{\mathrm{addn,wb}} = c_{\mathrm{addn,AcOH,tot}} = c_{\mathrm{addn,NaOAc,nom}} \frac{\rho}{\rho_{\mathrm{nom}}} \tag{A.15}$$

where ρ is density. For $\mathrm{pH_{nom}} = 4.5$, achieved by an $NaHCO_3$ addition without NaOAc, the added concentration under nominal conditions is computed as:

$$c_{\mathrm{addn,NaHCO_3,nom}} = -c_{\mathrm{H,appl}} + \frac{1}{c_{\mathrm{H,appl}}}\left(K_{\mathrm{w}} + \frac{K_{\mathrm{a,H_2CO_3}} K_{\mathrm{H,CO_2}} p_{\mathrm{CO_2,nom}}}{K_{\mathrm{hyd,CO_2}}}\left(1 + 2\frac{K_{\mathrm{a,HCO_3^-}}}{c_{\mathrm{H,appl}}}\right)\right) \tag{A.16}$$

After re-equilibration, this yields:

$$c_{\mathrm{addn,sa}} = c_{\mathrm{addn,AcOH,tot}} = 0 \tag{A.17}$$

$$c_{\mathrm{addn,wb}} = c_{\mathrm{addn,NaHCO_3,nom}} \frac{\rho}{\rho_{\mathrm{nom}}} \tag{A.18}$$

For the two formulations at $\mathrm{pH_{nom}} = 4.0$ and $\mathrm{pH_{nom}} = 4.5$, the in situ pH reported in Table 2 is then given by solving (with the above inputs and with all equilibrium constants evaluated at the test temperature ($T = 110$ °C).

Assuming a closed system that has been pre-equilibrated with the gases under their test partial pressures to give total C atom concentration $c_{\mathrm{C,tot}}$ and total S atom concentration $c_{\mathrm{S,tot}}$, the buffering capacity can be evaluated by implicit differentiation of (with respect to c_{H} to find the differential strong acid addition required to lower the pH by one unit. The resulting formula used to evaluate the buffering capacity reported in Table 2 is:

$$\beta_{\mathrm{closed}} = \ln 10 \left(c_{\mathrm{H}} \left(\begin{array}{l} 1 + c_{\mathrm{AcOH,tot}} \dfrac{K_{\mathrm{a,AcOH}}}{\left(K_{\mathrm{a,AcOH}} + c_{\mathrm{H}}\right)^2} \\ + \left(c_{\mathrm{C,tot}} - c_{\mathrm{CO_2}}\right) \dfrac{K_{\mathrm{a,H_2CO_3}}\left(c_{\mathrm{H}}^2 + K_{\mathrm{a,HCO_3^-}}\left(K_{\mathrm{a,H_2CO_3}} + 4c_{\mathrm{H}}\right)\right)}{\left(c_{\mathrm{H}}^2 + K_{\mathrm{a,H_2CO_3}}\left(c_{\mathrm{H}} + K_{\mathrm{a,HCO_3^-}}\right)\right)^2} \\ + c_{\mathrm{S,tot}} \dfrac{K_{\mathrm{a,H_2S}}}{\left(c_{\mathrm{H}} + K_{\mathrm{a,H_2S}}\right)^2} \end{array} \right) + \frac{K_{\mathrm{w}}}{c_{\mathrm{H}}} \right) \tag{A.19}$$

References

[1] NACE MR0175/ISO 15156, Petroleum and Gas Industries - Materials for Use in H2S Containing Environments in Oil and Gas Production, NACE International, Houston, TX, 2021.

[2] R.C. Newman, 2001 W.R. Whitney Award Lecture: Understanding the Corrosion of Stainless Steel, Corrosion 57 (2001) 1030–1041.

[3] R. Parrot, H. Pitts, Chloride Stress Corrosion Cracking in Austenitic Stainless Steel, Health and Safety Executive (HSE) Report RR902, 2011.

[4] E. Trillo, R.D. Kane, M. Maligas, M. Coles, E. Turbeville, Operational Limits for Austenitic Stainless Steels in H_2S-containing Environments, Corrosion 2006, Paper no. 156, NACE Int., Houston, 2006.

[5] J.-P. Audouard, M. Verneau, Evaluation of the Corrosion Resistance of High Nitrogen Containing Stainless Steels in Chloride and H_2S/CO_2 Environments, Corrosion 97, Paper no. 36, NACE Int., Houston, 2007.

[6] R. Case, Electrochemical Behavior of the Austenitic Stainless Steel Susceptibility to Sulfide Stress Cracking in H2S Containing Brines, Corrosion 2019, Paper 51319, NACE Int., Houston, 2019.

[7] G. Hinds, L. Wickström, K. Mingard, A. Turnbull, Impact of surface condition on sulphide stress corrosion cracking of 316L stainless steel, Corros. Sci. 71 (2013) 43–52.

[8] A. Turnbull, K. Mingard, J.D. Lord, B. Roebuck, D. Tice, K. Mottershead, N. Fairweather, A. Bradbury, Sensitivity of stress corrosion cracking of stainless steel to surface machining and grinding procedure, Corros. Sci. 53 (2011) 3398–3415.

[9] J.-S. Lee, Y. Kitagawa, T. Nakanishi, Y. Hasegawa, K. Fushimi, Effect of hydrogen sulfide ions on the passive behavior of type 316L stainless steel, J. Electrochem. Soc. 162 (2015) C685–C692.

[10] J. Ding, L. Zhang, M. Lu, J. Wang, Z. Wen, W. Hao, The electrochemical behaviour of 316L austenitic stainless steel in Cl-containing environment under different H_2S partial pressures, Appl. Surface Sci. 289 (2014) 33–41.

[11] Z. Wang, L. Zhang, X. Tang, Z. Zhang, M. Lu, The surface characterization and passive behavior of Type 316L stainless steel in H_2S-containing conditions, Appl. Surf. Sci. 423 (2017) 457–464.

[12] Z. Wang, L. Zhang, Z. Zhang, M. Lu, Combined effect of pH and H_2S on the structure of passive film formed on type 316L stainless steel, Appl. Surf. Sci. 458 (2018) 686–699.

[13] K. Ravindranath, B. Al-Wakaa, N.N. Tanoli, H.M. Shalaby, The effect of chloride-hydrogen sulfide synergism on the stress corrosion cracking susceptibility of type 321 stainless steel, Corrosion 73 (2017) 1268–1279.

[14] J. Hesketh, E. Dickinson, G. McMahon, A. Turnbull, G. Hinds, Influence of H_2S on the localised corrosion of 316L stainless steel, Part 1 – coupon testing, NPL Report MAT 92 (2020).

[15] S. Mat, R. Newman, Local Chemistry Aspects of Hydrogen Sulphide Assisted SCC of Stainless Steel, Corrosion 1994 Paper no. 228, NACE Int., Houston, 1994.

[16] P. Marcus, Sulfur-assisted corrosion mechanisms and the role of alloyed elements, in: P. Marcus (Ed.), Corrosion Mechanisms in Theory and Practice, Marcel Dekker, Inc., New York, 2002.

[17] G.S. Frankel, Pitting Corrosion of Metals: A Review of the Critical Factors, J. Electrochem. Soc. 145 (1998) 2186–2198.

[18] NACE TM0316-2016, Four-point Bend Testing of Materials for Oil and Gas Applications, NACE International, Houston, TX, 2016.

[19] NACE TM0177-2016, Laboratory Testing of Metals for Resistnace to Sulphide Stress Cracking and Stress Corrosion Cracking in H_2S Environments, NACE International, Houston, TX, 2016.

[20] MTDATA - Thermodynamics and Phase Equilibrium Software, Hampton Thermodynamics Ltd., Hampton, UK, 2020.

[21] J. Hesketh, P. Cooling, G. Hinds, Validation of oxygen purge techniques for stress corrosion cracking tests, NPL Report MAT 71 (2015).

[22] A. Kahyarian, S. Nesic, H_2S corrosion of mild steel: A quantitative analysis of the mechanism of the cathodic reaction, Electrochim. Acta 297 (2019) 676–684.

[23] J. Kittel, F. Ropital, F. Grosjean, E.M.M. Sutter, B. Tribollet, Corrosion mechanisms in aqueous solutions containing dissolved H_2S. Part 1: Characterisation of H_2S reduction on a 316L rotating disc electrode, Corros. Sci. 66 (2013) 324–329.
[24] J. Hesketh, E. Dickinson, A. Turnbull, G. Hinds, Influence of H_2S on the localised corrosion of 316L stainless steel, Part 2 – electrochemical testing, NPL Report MAT 94 (2020).
[25] S. Azuma, H. Tsuge, T. Kudo, T. Moroishi, Crevice corrosion of duplex stainless steel in simulated sour gas environments, Corrosion 45 (1989) 235–242.
[26] S. Azuma, T. Kudo, Crevice corrosion of corrosion-resistant alloys in simulated sour gas environments, Corrosion 47 (1991) 458–463.
[27] S.N. Smith, Current Understanding of Corrosion Mechanism Due to H_2S in Oil and Gas Production Environments, Corrosion 2015, Paper 5485, NACE Int., Houston, 2015.
[28] D. Rickard, G.W. Luther, Chemistry of iron sulfides, Chem. Rev. 107 (2007) 514–562.
[29] E. Wallqaert, T. Depover, I. De Graeve, K. Verbeken, FeS Corrosion Products Formation and Hydrogen Uptake in a Sour Environment for Quenched & Tempered Steel, Metals 8 (2018) 62.
[30] W.M. van Haaften, Private Communication, Shell Amsterdam, 2020.
[31] Y. Zheng, J. Ning, B. Brown, D. Young, S. Nesic, Mechanistic Study of the Effect of Iron Sulfides on Hydrogen Sulfide Corrosion of Carbon Steel, Corrosion 2015, Paper no. 5933, NACE Int., Houston, 2015.
[32] J. Amri, J. Kvarekvål, M. Tjelta, Modelling the Effect of Porous Iron Sulfide Layers on Sour Corrosion Behaviour, Corrosion 2019, Paper no. 13076, NACE Int., Houston, 2019.
[33] E.M. Gutman, G. Solovioff, D. Eliezer, The mechanochemical behavior of type 316L stainless steel, Corros. Sci. 38 (1996) 1141–1145.
[34] G. Wu, M.P. Singh, Effect of plastic deformation on pitting mechanism of SS304, Metall. Mater. Trans. A 50 (2019) 4750–4757.
[35] G. Sui, E.A. Charles, J. Congleton, The effect of delta-ferrite content on the stress corrosion cracking of austenitic stainless steels in a sulphate solution, Corros. Sci. 38 (1996) 687–703.
[36] G. Hinds, A. Turnbull, J. Hesketh, Role of H_2S in Localized Corrosion and Cracking of CRAs in Upstream Oil and Gas Applications, Corrosion 2017, Paper No 9463, NACE International, 2017.